ADVANCED FUNCTIONAL MATERIALS
www.afm-journal.de

Mesostructured Intermetallic Compounds of Platinum and Non-Transition Metals for Enhanced Electrocatalysis of Oxygen Reduction Reaction

*Xing-You Lang, Gao-Feng Han, Bei-Bei Xiao, Lin Gu, Zhen-Zhong Yang, Zi Wen, Yong-Fu Zhu, Ming Zhao, Jian-Chen Li, and Qing Jiang**

Alloying techniques show genuine potential to develop more effective catalysts than Pt for oxygen reduction reaction (ORR), which is the key challenge in many important electrochemical energy conversion and storage devices, such as fuel cells and metal-air batteries. Tremendous efforts have been made to improve ORR activity by designing bimetallic nanocatalysts, which have been limited to only alloys of platinum and transition metals (TMs). The Pt-TM alloys suffer from critical durability in acid-media fuel cells. Here a new class of mesostructured Pt–Al catalysts is reported, consisting of atomic-layer-thick Pt skin and Pt_3Al or Pt_5Al intermetallic compound skeletons for the enhanced ORR performance. As a result of strong Pt–Al bonds that inhibit the evolution of Pt skin and produce ligand and compressive strain effects, the Pt_3Al and Pt_5Al mesoporous catalysts are exceptionally durable and ≈6.3- and ≈5.0-fold more active than the state-of-the-art Pt/C catalyst at 0.90 V, respectively. The high performance makes them promising candidates as cathode nanocatalysts in next-generation fuel cells.

1. Introduction

Proton exchange membrane (PEM) fuel cell, which produces electricity from electrochemical oxidation of hydrogen with water as its product,[1,2] is an device alternative to environmentally unfriendly fossil-fuel use.[1,2] A major challenge to make PEM fuel cells commercially viable lies in the insufficient activity and durability of the materials that are employed at present as cathode catalysts for sluggish oxygen reduction reaction (ORR),[1–3] typically carbon-supported Pt nanoparticles (Pt/C).[1,3–6] Strong adsorption energies of O*, HO* and HOO* intermediates[2,3,7–9] and large electrochemical surface area (ECSA) loss in long-term operation of Pt/C[1,6–9] inevitably result in a low operating efficiency of the devices. Therefore, it is important to develop innovational materials with the ORR electrocatalytic activity and durability superior to that of Pt,[2,3,8–17] aiming at the significant reduction of the amount of Pt loaded in the cathodes,[2,3,8–12] or even replacing Pt-based catalysts with non-precious metals or metal-free materials.[13–17] Alloying technique is an attractive strategy,[2,3,8,9,18–21] by which ligand[19,22,23] and geometric effects[24,25] are introduced to alter chemical properties and make catalytic performance substantially different from the constituents.[26] Along Sabatier's principle, a number of Pt-based alloys with extended surface area (bulk) or various nanostructures have been developed by incorporating early (such as Sc,[27] Ti,[23] or Y[27]) or late (such as Fe,[18,28] Co,[18,29,30] Ni,[18,31–35] or Cu[25]) transition metals (TMs). These TM solute atoms at the subsurface modify the *d*-band structure (the center E_d and the width W_d) of the surface Pt atoms by virtue of the overlapping Pt-5*d* and TM-3*d* or –4*d* orbitals and the compressive/tensile strain effects,[2,3,8,9,22,24,26] that is, $E_d \propto -W_d^{1/2} \propto -V_{ddm}^{1/2} = -[\eta_{ddm}\hbar^2(r_{dPt}r_{dTM})^{3/2}/(mD_{Pt\text{-}TM}^5)]^{1/2}$ within the tight-binding approach.[22,26,36] Here V_{ddm} is the matrix element between Pt and TMs with the characteristic lengths r_{dPt} and r_{dTM} that are related to the spatial extent of their *d* orbitals, η_{ddm} is a dimensionless constant, *m* denotes the mass of an electron and $D_{Pt\text{-}TM}$ is their interatomic distance. The periodic properties of the *d* orbitals and the atomic radiuses of TMs downshift more or less the *d*-band center and thus weaken the O*, HO* and HOO* adsorption energies.[2,3,23,37–39] This enlists the Pt and 3*d* TM alloys with a Pt-skin structure, such as Pt_3TM/Pt (TM = Sc, Ti, Cr, Mn, Fe, Co, Ni, or Cu) systems, to exhibit the volcano-shaped specific activities as a function of atomic number. The highest value is obtained on Pt_3Ni/Pt[37–40] through adjusting the oxygen adsorption energies (ΔE_O) ~0.2 eV weaker than that of pure Pt (ΔE_O^{Pt}).[8,27] Although the alloying technique has thrown light on the design of ORR catalysts,[2,3,8,9,18–34] the previously intense research has been mainly limited to the highly

Prof. X.-Y. Lang, Dr. G.-F. Han, Dr. B.-B. Xiao, Dr. Z. Wen, Dr. Y.-F. Zhu, Dr. M. Zhao, Dr. J.-C. Li, Prof. Q. Jiang
Key Laboratory of Automobile Materials
Ministry of Education, and School of Materials Science and Engineering
Jilin University
Changchun 130022, China
E-mail: jiangq@jlu.edu.cn
Prof. L. Gu, Dr. Z.-Z. Yang
Beijing National Laboratory for Condensed Matter Physics
The Institute of Physics
Chinese Academy of Sciences
Beijing 100190, China

DOI: 10.1002/adfm.201401868

active catalysts of Pt and TMs in the 3*d* series, typically Pt_3Fe, Pt_3Co and Pt_3Ni.[18,28–42] These alloys suffer from the severe degradation of catalysis and stability during the voltage cycling in acid as a consequence of the continuous dissolution of TM atoms.[8,9,41,42] Even in the Pt-skin structure,[2,3,8,9,39,41,42] the protection of pure Pt layer on the outermost surface does not evidently alleviate the TM dissolution because of the low formation energy of Pt-TM alloys,[43] which intrinsically results in the instability on thermodynamic grounds[44] and is insufficient to inhibit the inter-diffusion of Pt and TM atoms in both interior and shell,[45] in particular, of nanostructures[46] (see the details on theoretical demonstrations in the Supporting Information). In this regard, it is highly desirable to look beyond the Pt-TM systems and explore novel alloys that simultaneously show extraordinary activity and durability.

Here we report a new set of high-temperature intermetallic compounds of platinum and aluminum (Pt_xAl, $x = 3$ or 5) with a bimodal mesoporous (MP) structure consisting of atomic-layer-thick Pt skin and thermodynamically stable Pt_3Al or Pt_5Al subsurface (MP Pt_3Al/Pt or Pt_5Al/Pt) for the high-performance ORR electrocatalysis. The choice of Al in the development of Pt-based catalysts for PEM fuel cells is motivated by its location in the Periodic Table on the amphoteric/metalloid line and the low cost. Amphoteric properties of Al and large electronegativity difference between Al and Pt enable both Al-3*p*/Pt-5*d* hybridization and compressive strain to alter the *d*-band structures of surface Pt atoms on MP Pt_3Al/Pt and Pt_5Al/Pt, offering the specific activities ≈6.3- and ≈5.0-fold higher than Pt/C nanocatalyst at 0.90 V, respectively. Meanwhile, the strong Pt–Al covalent bonds at Pt_xAl/Pt-skin interface significantly suppress the evolution of Pt skin and thus enhance the stability against the further dissolution of Al, enlisting MP Pt_xAl/Pt catalysts to exhibit extraordinary structural stability. The enhanced ORR catalytic activity and durability as well as the reduced cost due to the incorporation of Al make such MP Pt_3Al/Pt and Pt_5Al/Pt intermetallic compounds promising candidates as cathode nanocatalysts in next-generation PEM fuel cells.

2. Results and Discussion

Our strategy to mass-produce mesostructured Pt_xAl/Pt intermetallic compounds is realized by a facile procedure, viz. alloying pure Pt and Al, and then dealloying the alloy ribbons (see Experimental Section and Supporting Information Figure S1a,b).[47–51] The precursor of $Pt_{12}Al_{88}$ (at%) ribbons with a cross section of ≈20 μm × ≈1 mm is firstly produced by single-roller melt-spinning in vacuum from its ingot (Figure S1a,c,d),[48,49] which is composed of a uniform α-Al metal and Pt_8Al_{21} alloy intermixture (Figure S2). Through dealloying in 1 M NaOH aqueous solution at room temperature (Figure S1b), the α-Al in the mixture is rapidly dissolved from the entire ribbons. In the already etched Pt_8Al_{21} alloy, the less noble Al component is further selectively dealloyed at a slow rate for the production of thermodynamically stable MP Pt_3Al/Pt intermetallic compound without any loss of noble metal (Figure S3).[49,51] **Figure 1**a shows representative top-view scanning electron microscope (SEM) image of the mesostructured Pt_3Al/Pt, demonstrating a bimodal MP architecture consisting of quasi-periodic Pt_3Al/Pt ligaments and MP channels with

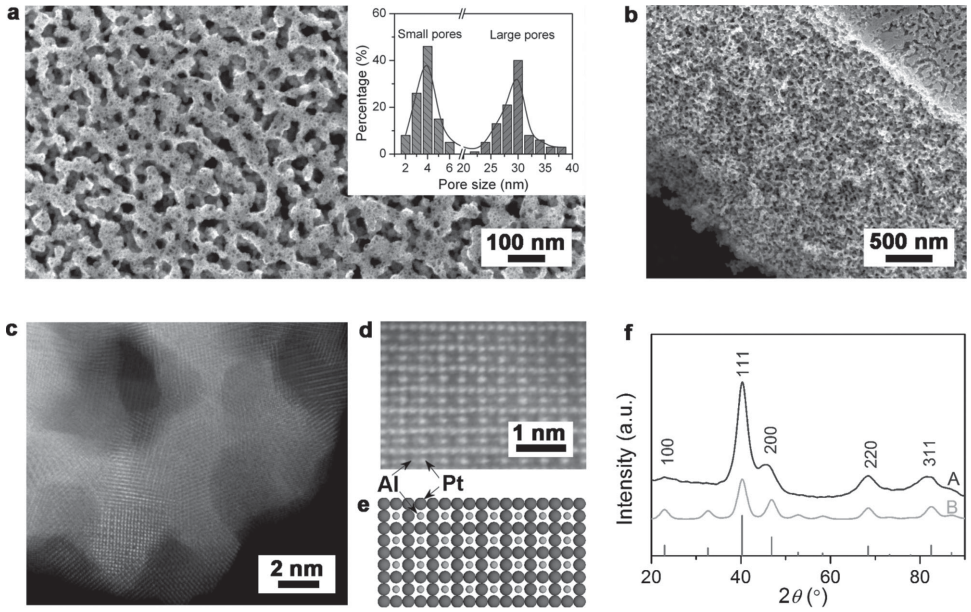

Figure 1. Microstructure characterization of MP Pt_3Al/Pt. a) Top-view and, b) cross-sectional SEM images of as-dealloyed MP Pt_3Al/Pt ribbons with a bimodal nanoporosity consisting of small pores of ≈4 nm and large channels of ≈30 nm. Inset: Distributions of small and large pore sizes. c) HAADF-STEM image of MP Pt_3Al/Pt intermetallic compound, showing that the interconnecting Pt_3Al/Pt ligaments with a size of ≈4 nm comprise various surface structures with a small fraction of undercoordinated step, corner and edge sites. d) Magnified atomic-resolution HAADF-STEM image of Pt_3Al with super lattice feature, confirming the FCC $L1_2$ structure of intermetallic Pt_3Al compound under a Pt monolayer. e) Atomically structural model with a (110) surface based on (d) for computational simulation. f) XRD patterns of A) MP Pt_3Al fabricated by chemical dealloying and B) the simulated structure model of (e). The line pattern shows reference card 65–3255 for Pt_3Al intermetallic compound according to JCPDS.

Adv. Funct. Mater. **2014**,
DOI: 10.1002/adfm.201401868

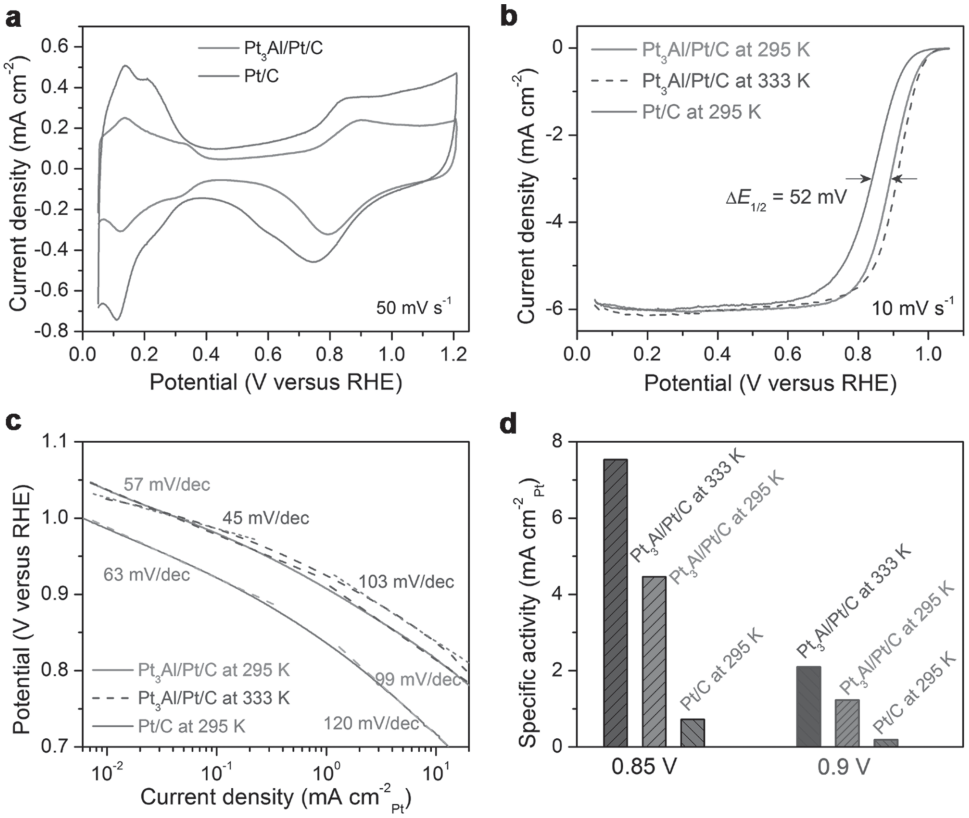

Figure 2. Electrochemical characterization of MP $Pt_3Al/Pt/C$. a) CV curves of MP $Pt_3Al/Pt/C$ and Pt/C (20% by weight of ≈3 nm Pt nanoparticles) electrodes recorded in N_2-purged 0.1 M $HClO_4$ aqueous electrolyte at a scan rate of 50 mV s^{-1}. b) Polarization curves for the ORR of MP $Pt_3Al/Pt/C$ and Pt/C in O_2-saturated 0.1 M $HClO_4$ solution at 295 and 333 K with a scan rate of 10 mV s^{-1} and a rotation rate of 1600 rpm. c) Tafel plots showing the kinetic current density of MP $Pt_3Al/Pt/C$, Pt/C as a function of the potential versus RHE. d) Comparison of specific kinetic activity (ECSA kinetic-current density) for MP $Pt_3Al/Pt/C$ relative to Pt/C at 0.85 and 0.90 V versus RHE.

characteristic lengths of ≈4 and ≈30 nm (inset of Figure 1a). The dissolution of Al reduces the thickness of the dealloyed ribbon to ≈4 μm (Figure 1b). Scanning transmission electron microscope (STEM) energy-dispersive spectroscopy (EDS) mapping shows a uniform distribution of Al atoms in Pt matrix with a slightly low concentration at the rims of the skeletons (Figure S4), implying the formation of a Pt_3Al/Pt core/shell structure. Top-view and cross-section atomic-resolution high-angle annular-dark-field (HAADF) STEM images illustrate the structural feature that the interconnected ligaments mainly comprise atomic-layer-thick Pt(111) skin and ≈4-nm polycrystalline Pt_3Al subsurface (Figure 1c and Figure S5). The FCC $L1_2$ structure of intermetallic Pt_3Al compound can be directly identified from HAADF-STEM image along the [001] zone axis (Figure 1d), where a periodic square array of pure Al columns (low intensity) is surrounded by Pt columns (high intensity) at the edges and corners of each unit cell (Figure 1d,e). The super ordered structure of MP Pt_3Al intermetallic compound is further verified by X-ray diffraction (XRD) pattern, in which the obvious diffraction peaks correspond to the (100), (111), (200), (220) and (311) planes of FCC phase in space group Pm-3m (no. 221) (JCPDS 65–3255) (Figure 1f). The broadened peaks are attributed to the nanoscale polycrystals.

To assess the electrocatalysis of $Pt_3Al/Pt/C$ intermetallic compound, the catalyst ink is loaded onto glassy carbon electrode for electrochemical measurements. **Figure 2**a shows the cyclic voltammetry (CV) curve in a nitrogen-purged 0.1 M $HClO_4$ solution at room temperature. Resembling the observation of Pt/C catalyst,[4,39,40] the CV profile of MP $Pt_3Al/Pt/C$ exhibits two Pt(111) characteristics. These include the H_{upd} adsorption/desorption processes ($H^+ + e^- = H_{upd}$) in $0.05 < E < 0.4$ V and the formation of an OH_{ad} layer ($2H_2O = OH_{ad} + H_3O^+ + e^-$) in $E >$ 0.7 V, electrochemically confirming the $Pt_3Al/Pt(111)$ core/shell structure.[4,18,39,40] Here E is the potential versus the reversible hydrogen electrode (RHE). The ECSA of MP $Pt_3Al/Pt/C$ is calculated to be ≈3.9 cm^2 from the charge taking to adsorb/desorb monolayer of hydrogen in the H_{upd} region after double-layer correction and assuming a value of ≈210 μC cm^{-2} for the adsorption of a hydrogen monolayer.[4,39,40] Careful inspection of the CV profile reveals that there are ≈50 mV positive shifts in the OH_{ad} absorption/desorption peaks for MP $Pt_3Al/Pt/C$ relative to Pt/C with the ECSA of ≈6.7 cm^2 (Figure 2a). This finding indicates that the OH_{ad} surface sites on the Pt(111) skin of MP Pt_3Al are weakened in comparison with that of Pt/C.[8,23,39]

The ORR experiments are performed using a rotating disk electrode (RDE) in O_2-saturated 0.1 M $HClO_4$ solution at 295 and 333 K with a scan rate of 10 mV s^{-1}. Figure 2b shows the typical polarization curves in a potential window from 0.05 to 1.05 V versus RHE for MP $Pt_3Al/Pt/C$ and Pt/C at a rotation rate of 1600 rpm. Both catalysts exhibit two distinguishable potential

regions: a well-defined diffusion control region (E < 0.7 V), in which the current density reaches its diffusion-limited value of ≈6.0 mA cm^{-2}, and a mixed kinetic-diffusion region (0.7 < E < 1.0 V), where the current density increases exponentially as mass transport plays an increasingly important role. In the mixed region, there is a remarkably positive shift of ≈52 mV in the half-wave potential ($\Delta E_{1/2}$) for MP Pt_3Al/Pt/C relative to that of Pt/C at 3.0 mA cm^{-2}, which means a significant enhancement of the ORR activity in this super ordered structure.[29,34,39] To evaluate the intrinsic activity, their ECSA kinetic current densities are calculated according to the Koutecky-Levich (K-L) equation (Figure 2c).[29,52,53] The specific activities of MP Pt_3Al/Pt/C at 295 K reach ≈4.46 and ≈1.23 mA cm$^{-2}_{Pt}$ at 0.85 and 0.90 V, respectively, which are ≈6.2 and ≈6.3 times higher than that of Pt/C catalyst (≈0.725 and ≈0.195 mA cm$^{-2}_{Pt}$) (Figure 2d). When increasing the temperature from 295 to 333 K, the specific activities increase to ≈7.53 and ≈2.10 mA cm$^{-2}_{Pt}$ at 0.85 and 0.90 V (Figure 2c,d). The superior ORR activities of the MP Pt_3Al/Pt/C at 295 and 333 K are also gleaned from smaller Tafel slopes (≈57 and ≈45 mV/decade) than that of Pt/C (≈63 mV/decade) at low overpotentials (Figure 2c).[30] The mass-transport-limited current density increases with the rotation rate, as demonstrated by the rotation-rate-dependent polarization curves in Figure S6a (Supporting Information). In the corresponding K-L plot (j^{-1} versus $\omega^{-1/2}$) at 0.725–0.800 V (Figure S6b),[4,14,29,30,53] the good linearity and parallelism indicate a first-order reaction kinetics with respect to molecular oxygen. The electron transfer number (n) of ≈4.0 suggests the nearly complete reduction of O_2 to H_2O on the surface of MP Pt_3Al/Pt/C via a four-electron reaction process.[14,29] The enhancement of electrocatalytic activity implies that the Pt(111) skin on Pt_3Al ligaments possesses surface electronic properties more favorable for the ORR. Instead of discrete particles supported by high-surface-area carbon, a continuous Pt_3Al/Pt film with a MP architecture directly integrated with current collector of the cathode is anticipated to exhibit much higher electrocatalytic activity because of the mesostructure, which bridges the extended surfaces with superior activity and the nanoscale structures with high specific surface area (Figure 1a,b).[10,39,54,55]

Although there is a thermodynamic force toward the dissolution of Al (the standard dissolution potential of –1.66 V versus RHE for Al to Al^{3+}) under the acidic conditions,[27,56,57] the formation of Pt skin on the surface of Pt_3Al intermetallic compound with an exceptionally negative heat of formation (≈–2.8 eV)[42] provides the stability against the Al dissolution from the interior of compound, and enables more durable performance.[2,3,8,9,35,39,40] As shown in Figure S7 (Supporting Information), even after 10 000 cycles, the MP Pt_3Al/Pt/C shows a degradation of only ≈6 mV in the half-wave potential, much smaller than that of Pt/C (≈10 mV). Furthermore, there is not obvious morphology change and only ≈3.7% Al dissolves from the Pt_3Al/Pt/C catalyst (Figure S8). The influence of thermodynamic instability on the durability can be alleviated by adjusting Pt_xAl/Pt intermetallic compound with less Al content in the subsurface, such as Pt_5Al/Pt/C, although this may result in a slight reduction in electrocatalytic activity (≈0.969 mA cm$^{-2}_{Pt}$, ≈5.0-fold enhancement relative to that of Pt/C) in comparison with Pt_3Al/Pt/C.

By consecutively chemical dealloying $Pt_{12}Al_{88}$ ribbon precursor in 1 M NaOH aqueous solution firstly at room temperature for 20 min and then at 95 °C for 90 min, the reaction-diffusion process produces a bimodal MP Pt_5Al/Pt(111) core/shell structure with slightly larger characteristic lengths (**Figure 3**a and Supporting Information Figure S9,10). Its XRD peaks corresponding to (111), (200), (220), (311), (222), (400), and (331) planes are consistent with these of Pt_5Al intermetallic compound with FCC structure (JCPDS 65–8157) (Figure 3b). To estimate the durability of MP Pt_5Al/Pt, the accelerated stability tests are performed by the continuous potential cycling between 0.6 and 1.1 V versus RHE at a scan rate of 50 mV s^{-1} in an O_2-saturated 0.1 M $HClO_4$ solution. The ORR polarization curves on MP Pt_5Al/Pt/C before and after the stability test of 40,000 cycles are shown in Figure 3c, exhibiting the superior stability over Pt/C catalyst (Figure S11a). As demonstrated in the plot for $\Delta E_{1/2}$ as a function of cycle number (Figure 3d), MP Pt_5Al/Pt/C shows only ≈4-, 11-, 18- and 20-mV degradations in the half-wave potential after each 10 000th cycle, much smaller than these of Pt/C ($\Delta E_{1/2}$ ≈ 10, 15, 37 and 75 mV). This is consistent with the ECSA measurements, which are evaluated according to the H_{upd} adsorption/desorption region in the CV curves (Figure 3e and Figure S11b). The ECSA of MP Pt_5Al/Pt/C remains ≈66%, in distinct contrast with a large loss of ≈60% for Pt/C (Figure 3f) due to the Ostwald ripening and aggregation of the Pt nanoparticles driven by the high surface/volume ratio (Figure S12).[1,3,35,55] For comparison, the $\Delta E_{1/2}$ and ECSA of MP Pt_3Al/Pt/C are also included in Figure 3d,f, respectively. Owing to more Al content, Pt_3Al/Pt/C represents a slight instability in comparison with MP Pt_5Al/Pt/C. This is also validated by the chemical characterization which demonstrates the Al dissolution from Pt_5Al/Pt/C (≈2.2%) is lower than Pt_3Al/Pt/C (≈3.7%) after 10 000 cycles (Figure S8b,13b).

Under the premise that the enhanced ORR performance of Pt_xAl/Pt intermetallic alloys could be qualitatively explained by the catalytic knowledge established on their bulks,[27,39] density functional theory (DFT) calculations are employed to theoretically elucidate the physical picture. The Pt_3Al/Pt(111), Pt_5Al/Pt(111) and Pt(111) periodic supercells (**Figure 4**a) are constructed with the same lattice parameters (3.878, 3.896, and 3.924 nm) and XRD patterns as these of experimental measurements (Figure 1f, 3b).[27] Figure 4b illustrates the partial density of states (PDOS) for each electron of Al-3*s*, Pt-6*s* and Al-3*p*, Pt-5*d* in Pt_3Al. The formation of intermetallic Pt–Al bond with exceptionally negative formation heat of ≈–0.74 eV/atom[43] gives rise to obvious electron localization function (Figure S14, Supporting Information) and definite negative shift (≈–0.51 eV) of Pt-4*f* X-ray photoelectron spectroscopy spectra (Figure 4c) for Pt_3Al and Pt_5Al relative to Pt/C. The negative shift in binding energy roots in a net result of both ligand and compressive strain effects in MP Pt_3Al and Pt_5Al,[58,59] which would jointly lead to the downshift of *d*-band center,[19,22–26] because of a primary role of the former.[60–62] This is different from the observation in the Pt-based alloys with the negligible ligand effect, where a positive shift of the core level is accompanied by a downshift of *d*-band center as a result of the compressive strain.[12,63] Therefore, the strong Pt–Al covalent bonds not only enable the excellent kinetic stability (Figure 3 and Supporting Information Figure S7)[8,9,27,43] but also produce the hybridization between the Al-3*p* states and the Pt-5*d* states,[36] substantially altering the *d* band of surface Pt atoms on Pt_xAl/Pt(111)

DOI: 10.1002/adfm.201401868

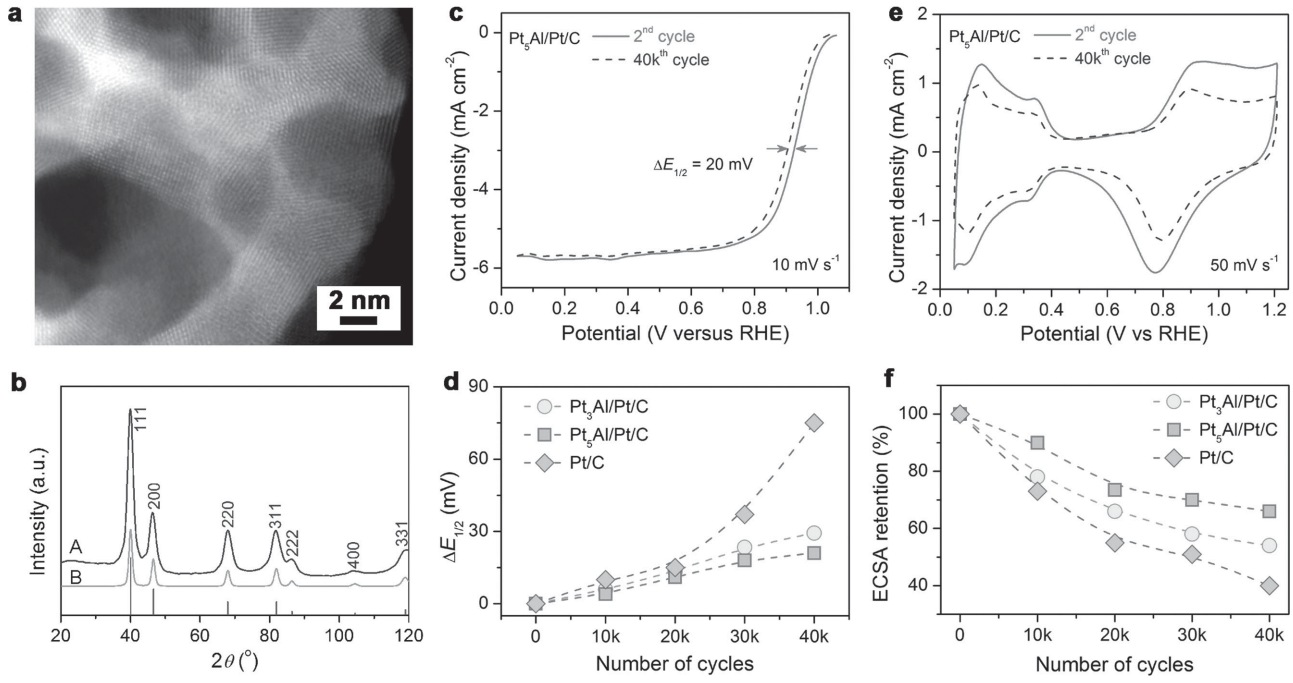

Figure 3. STEM image and electrochemical stability of MP Pt_5Al/Pt/C. a) HAADF-STEM image of MP Pt_5Al/Pt intermetallic compound dealloyed in NaOH aqueous solution, showing the microstructure with a bimodal nanoporosity. b) Measured (A) and simulated (B) XRD patterns of MP Pt_5Al/Pt, corresponding to the line pattern for FCC Pt_5Al intermetallic compound (JCPDS PDF 65–8157). c) Polarization curves for the ORR of MP Pt_5Al/Pt/C catalyst before and after 40,000 potential cycles, collected in O_2-saturated 0.1 M $HClO_4$ aqueous solution at room temperature with a rotation rate of 1600 rpm and a scan rate of 10 mV s^{-1}. d) Half-wave potentials for Pt_3Al/Pt/C, Pt_5Al/Pt/C and Pt/C catalysts as a function of number of cycles. e) CV curves in N_2-purged 0.1 M $HClO_4$ aqueous solution at room temperature and 50 mV s^{-1} for MP Pt_5Al/Pt/C catalyst before and after 40 000 potential cycles in a range from 0.6 to 1.1 V. f) Comparison of ECSA retentions for Pt_3Al/Pt/C, Pt_5Al/Pt/C and Pt/C catalysts during the electrochemical cycling.

relative to that of Pt(111).[2,3,19] The remarkable downshift of *d*-band center of Pt_3Al/Pt(111) (≈0.16 eV) weakens the adsorption energies of O* and HO* by ≈0.18 and ≈0.12 eV relative to these of Pt(111) (Figure 4d),[8,23,26,39] very close to their most appropriate values (≈0.2 and ≈0.1 eV) required for the highest specific activity,[8,27] respectively. The decrease of adsorption energies makes the adsorbed HOO* instable, and it is easy to break the Pt-OH bonds (Figure 2a).[8,9,23,39] As illustrated in the free-energy diagram (Figure S15), the free-energy change for the formation of adsorbed HOO* (ΔG_1) increases to 0.11 eV, while the one for the removal of HO* (ΔG_2) decreases to 0.02 eV. Therefore, the rate-limiting step in ORR changes to the formation of HOO* on Pt_3Al/Pt(111) with $\Delta G_{max} = \Delta G_{1\text{-}Pt3Al/Pt(111)} = 0.11$ eV from the removal of HO* on Pt(111) with $\Delta G_{max} = \Delta G_{2\text{-}Pt(111)} = 0.15$ eV (inset of Figure S15),[7] where the subscript *max* denotes the maximum. On the basis of assumption that the activation barrier for the rate-limiting proton-transfer step is equal to ΔG_{max},[7] the enhancement factor of specific activity is approximately accessed to be ≈4.7 relative to Pt(111). Owing to the dependence on the compositional profile, the *d*-band center of surface Pt atoms on subsurface Pt_5Al intermetallic alloy (–2.49 eV) falls in between these of Pt(111) and Pt_3Al/Pt(111) (Figure 4d),[8,19,23] and thus the activity enhancement is little lower than that of Pt_3Al/Pt. Compared with the theoretical values for bulks, the further enhancements of catalytic activity experimentally observed in MP Pt_3Al/Pt and Pt_5Al/Pt originate from the advantages offered by the bimodal MP architecture. This unique sponge structure produces high surface area while achieving the intermetallic compound skeletons with both the desirable compositional profile and the structure of atomic-layer-thick Pt skin.[52,54] In addition, the interconnective and bimodal channels enable the confinement effect in the large pores and the electric-double-layer overlap (EDL) effect in the small ones.[54,58] The former makes the trapped molecules remain close to the electrode surface and prevents them from escaping to bulk solution for the efficient electrochemical reaction, whereas the latter alters the EDL potential distribution and enhances the electrocatalytic performance.[64]

As a function of the atomic number of solute metals, the enhancements of specific activities for a number of typical Pt-based alloys relative to Pt/C are plotted in Figure 4e. Here the maximal values of nanostructured Pt_3TM/Pt (TM = Ti,[38] Cr,[37] Mn,[37] Fe,[28] Co,[29] Ni,[33] Cu,[25] Y,[38] and Zr[38]) are included for comparison. In contrast with the general volcano shape for alloys of Pt and TM elements in the fourth and fifth periods,[8,23,27,40] the intermetallic compound of Pt and Al in the third period exhibits the activity enhancement comparable to the maxima reported in Pt_3TM systems, such as Pt_3Ni/Pt[33] and Pt_3Y/Pt.[38] This evidently demonstrates the importance of controlling fundamental properties by alloying technique.[22,26,36] As shown in Pt–Al systems, not only do the strong Pt–Al covalent bonds enhance the durability, but the hybridization of Al-3*p* and Pt-5*d* gives rise to the downshift of the *d*-band center, which adjusts the adsorption energy to change the rate limiting step and improve the ORR reaction. Complementing Pt_3Al in the Pt_3TM systems provides a proof of concept that extending the exploration beyond Pt_3TM systems

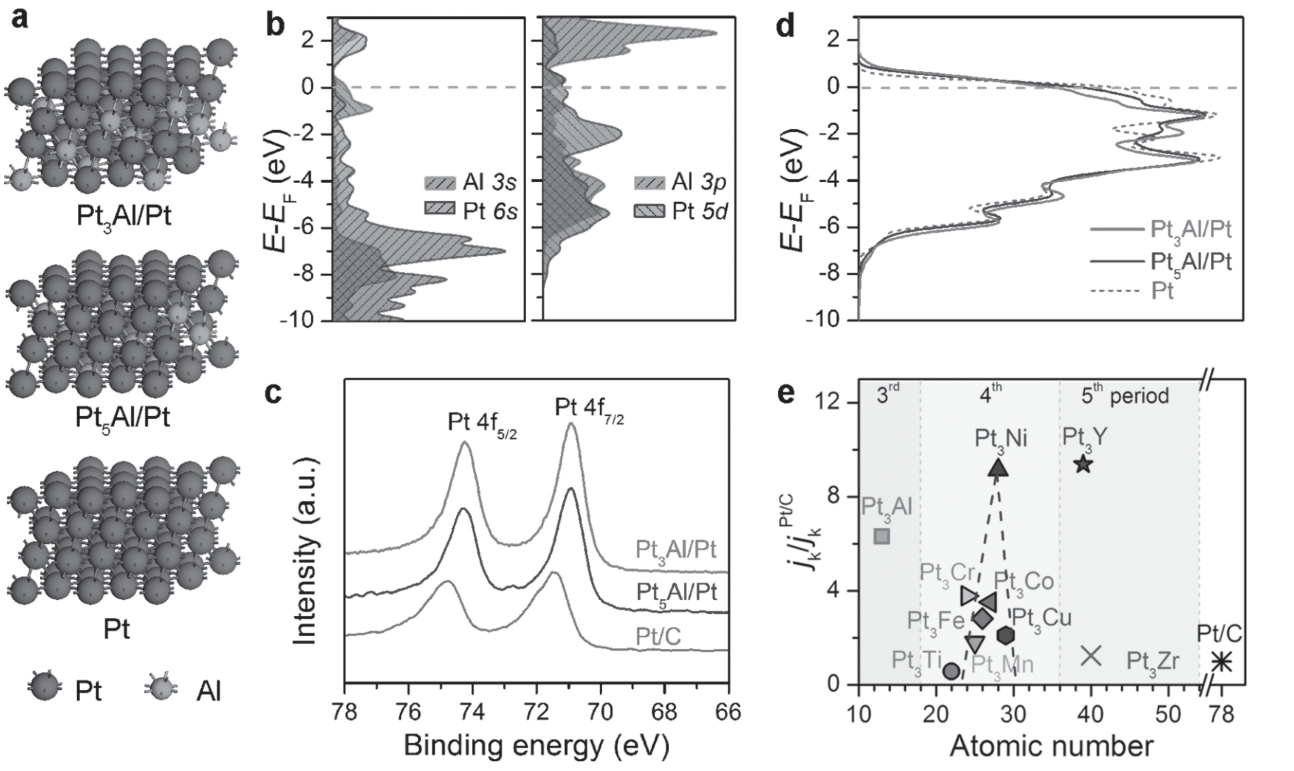

Figure 4. Theoretical calculations of the dealloyed Pt_xAl/Pt compounds. a) The atomic structures of the dealloyed Pt_3Al/Pt (top) and Pt_5Al/Pt (middle) that consist of Pt skin and show the same XRD patterns as the experimental ones. Bottom: The atomic structure of pure Pt. b) The typical partial density of states for each Al-*3s*, Pt-*6s* and Al-*3p*, Pt-*5d* electron in Pt_3Al/Pt bulk, illustrating the formation of intermetallic Pt–Al bonds. c) High-resolution XPS spectra of Pt 4*f* for Pt_3Al, Pt_5Al and Pt/C catalysts. d) The local density of states of Pt skins on intermetallic Pt_3Al and Pt_5Al compounds in comparison with pure Pt, demonstrating their evolution of d-band centers. e) Comparison of specific activity enhancement ($j_k/j_k^{Pt/C}$) for Pt_3Al/Pt intermetallic compound and the maximal values reported for Pt_3TM (TM = Ti,[38] Cr,[37] Mn,[37] Fe,[28] Co,[29] Ni,[33] Cu,[25] Y,[38] and Zr[38] nanostructures versus the state-of-the-art Pt/C catalyst at 0.90 V in 0.1 M $HClO_4$.

allows the development of novel alloy catalysts with exceptionally high performance for the ORR.

3. Conclusions

In summary, we have developed a new class of Pt_xAl intermetallic compound catalysts with bimodal mesoporous architectures and tunable compositional profiles by a facilely and cost-effectively alloying/dealloying approach for the high-performance ORR. Besides the remarkable reduction in Pt-loading, the MP Pt_3Al/Pt and Pt_5Al/Pt compounds are tailored to exhibit significantly enhanced ORR kinetics and durability in comparison with the present state-of-the-art Pt/C catalyst. The ORR kinetic activities of MP Pt_3Al/Pt/C and Pt_5Al/Pt/C are enhanced relative to Pt/C by a factor of ~6.3 and ~5.0 at 0.90 V, respectively. DFT calculations have demonstrated that the impressive ORR performance of the new intermetallic compound catalysts originates from the unique architecture and compositional profiles in the skeletons, viz. the atomic-layer-thick Pt skin and intermetallic Pt_3Al or Pt_5Al core, wherein both ligand and strain effects give rise to the downshift of *d*-band center and thus weaken the adsorption of oxygenated species. This exploration of Pt_xAl intermetallic compounds provides a new design strategy for developing novel fuel-cell catalysts beyond Pt-TM systems with both excellent electrocatalytic activity and stability.

4. Experimental Section

Fabrication of MP Pt_3Al/Pt and Pt_5Al/Pt Intermetallic Compounds: The precursor $Pt_{12}Al_{88}$ (at%) ribbons with a cross section of ≈20 μm × ≈1 mm were produced by a melting-spinning method in a high-purity argon gas atmosphere from its ingot that was made by arc melting using pure Pt (99.99%) and Al (99.95%) in vacuum.[35,48,49] The free-standing MP Pt_3Al/Pt intermetallic compound was synthesized by chemical dealloying the as-prepared $Pt_{12}Al_{88}$ ribbons in N_2-bubbled 1 M NaOH aqueous solution at 25 °C. The fabrication of MP Pt_5Al/Pt was carried out by consecutively chemical dealloying firstly at room temperature for 20 min and then at 95 °C for 90 min. The dealloyed samples were rinsed in pure water (18.2 MΩ cm) more than five times to remove chemical substances in MP channels.

Structural Characterization: The microstructure and chemical composition of the specimens were investigated using a field-emission scanning electron microscope (JSM-6700F, JEOL, 15 keV) equipped with an X-ray energy-dispersive spectroscopy (EDS). High-resolution scanning transmission electron microscopy (STEM) and STEM-EDS element mapping characterizations were performed on a field-emission transition electron microscope (JEM-ARM200CF, JEOL) operated at 200 keV and equipped with double spherical-aberration correctors for both condenser and objective lens. X-ray diffraction measurements were carried out on a D/max2500pc diffractometer using Cu K_α radiation.

DOI: 10.1002/adfm.201401868

X-ray photoelectron spectroscopy characterization was performed on Thermo ECSALAB 250 with an Al anode.

Electrochemical Measurements: After crushing MP ribbons by intense tip sonication in a solution of Nafion (0.05% v/v, Sigma Aldrich), isopropanol (20.95% v/v) and water (79% v/v), the catalyst inks of MP Pt_3Al/Pt/C or Pt_5Al/Pt/C with a concentration of 0.4 mg mL^{-1} were prepared by mixing with carbon black (Vulcan XC-72, Cabot) and sonicating for 30 min. Approximately 10-μL as-prepared MP Pt_3Al/Pt/C or Pt_5Al/Pt/C inks and commercial Pt/C (20 wt%, Johnson Matthey) were drop-cast onto a 5-mm-diameter glassy carbon rotating disk electrode (RDE, Pine Research Instrumentation) served as working electrode. All electrochemical experiments were carried out in a three-electrode electrochemical cell by employing a Pt foil electrode as the counter electrode, and a saturated calomel electrode (Hg/Hg_2Cl_2, SCE) as the reference electrode. All potentials were calibrated with respect to a reversible hydrogen electrode (RHE). ECSA was characterized by cyclic voltammetry over a potential range from 0.05 V to 1.20 V (RHE) at a scan rate of 50 mV s^{-1} in N_2-saturated 0.1 M $HClO_4$ solution. ECSA values of all specimens were calculated by integrating the areas of the hydrogen adsorption/desorption region (0.05–0.4 V) after the conventional double-layer correction and using a conversion factor of ≈210 μC cm^{-2}. The ORR measurements were performed in O_2-saturated 0.1 M $HClO_4$ solution at a rotation rate of 1600 rpm and a scan rate of 10 mV s^{-1} over the potential range from 0.05 to 1.05 V (RHE). The kinetic current density (j_k) was calculated according to Koutecky-Levich equation[29,52,53]

$$1/(A_{geo}j_m) = 1/(A_{Pt}j_k) + 1/(A_{geo}j_d) = 1/(A_{Pt}j_k) + 1/(0.62nFA_{geo}D^{2/3}\nu^{-1/6}\omega^{1/2}C_{O_2})$$

where j_m is the measured current density, and j_d is the diffusion limited current density, n is the number of electrons transferred, F is the Faraday constant (96 485 C mol^{-1}), A_{geo} is the area of the electrode (0.196 cm^2), D is the diffusion coefficient of O_2 in 0.1 M $HClO_4$ solution (1.93×10^{-5} cm^2 s^{-1}), ν is the viscosity of the electrolyte (1.01×10^{-2} cm^2 s^{-1}), $\omega = 2\pi f/60$ is the angular frequency of rotation at a rate f in r.p.m. and C_{O2} is the concentration of molecular oxygen in 0.1 M $HClO_4$ solution (1.26×10^{-6} mol cm^{-3}).

Computational Methods: All the Density Functional Theory (DFT) calculations on Pt_3Al and Pt_5Al were performed on periodical ($\sqrt{12} \times \sqrt{12}$) R 30° four-layer supercells, respectively, using DMol^3 code by a spin-unrestricted method, except that the bonding nature was investigated by electron localization function in CASTEP code with ultrasoft pseudopetentails.[27] A 30 Å-thick vacuum was added along the direction perpendicular to the surface, and the topmost layer and the adsorbates were allowed to relax while the other atoms were fixed. The k points were set as 2 × 2 × 1 and the dipole slab correction was applied. The DFT Semi-core Pseudopots (DSPP) method was implemented for relativistic effects, in which core electrons was approximated by a single effective potential and introduced by some degree of relativistic correction into the core. The double numerical atomic orbital augmented by a polarization function was set as the basis. Exchange and correlation effects were described by the generalized gradient approximation with the Perdew–Burke–Ernzerhof functional (PBE). The accurate electronic convergence was achieved with a smearing of 0.136 eV to the orbital occupation. A conductor-like screening model (COSMO) was used to simulate a H_2O solvent environment throughout the whole process.

Supporting Information

Supporting Information is available from the Wiley Online Library or from the author.

Acknowledgments

X.Y.L., G.F.H., and B.B.X. contributed equally to this work. This work was supported by the National Key Basic Research Development Program (Nos.No. 2010CB631001), the National Natural Science Foundation of China (No. 51201069, 51422103), the Keygrant Project of Chinese Ministry of Education (No. 313026), the Program for New Century Excellent Talents in University (No. NCET-10–0437), and the Research Fund for the Doctoral Program of Higher Education of China (No. 20120061120042).

Received: June 7, 2014
Revised: October 12, 2014
Published online:

[1] R. Borup, J. Meyers, B. Pivovar, Y. S. Kim, R. Mukundan, N. Garland, D. Myers, M. Wilson, F. Garzon, D. Wood, P. Zelenay, K. More, K. Stroh, T. Zawodzinski, J. Boncella, J. E. McGrath, M. Inaba, K. Miyatake, M. Hori, K. Ota, Z. Ogumi, S. Miyata, A. Nishikata, Z. Siroma, Y. Uchimoto, K. Yasuda, K. I. Kimijima, N. Iwashita, *Chem. Rev.* **2007**, *107*, 3904.
[2] M. K. Debe, *Nature* **2012**, *486*, 43.
[3] H. A. Gasteiger, S. S. Kocha, B. Sompalli, F. T. Wagner, *Appl. Catal. B Environ.* **2005**, *56*, 9.
[4] K. J. J. Mayrhofer, B. B. Blizanac, M. Arenz, V. R. Stamenkovic, P. N. Ross, N. M. Markovic, *J. Phys. Chem. B* **2005**, *109*, 14433.
[5] O. Antoine, Y. Bultel, R. Durand, *J. Electroanal. Chem.* **2001**, *499*, 85.
[6] P. J. Ferreira, G. J. la O', Y. Shao-Horn, D. Morgan, R. Makharia, S. Kocha, H. A. Gasteiger, *J. Electrochem. Soc.* **2005**, *152*, A2256.
[7] J. K. Nørskov, J. Rossmeisl, A. Logadottir, L. Lindqvist, J. R. Kitchin, T. Bligaard, H. Jónsson, *J. Phys. Chem. B* **2004**, *108*, 17886.
[8] I. E. L. Stephens, A. S. Bondarenko, U. Grønbjerg, J. Rossmeisl, I. Chorkendorff, *Energy Environ. Sci.* **2012**, *5*, 6744.
[9] Y. H. Bing, H. S. Liu, L. Zhang, D. Ghosh, J. J. Zhang, *Chem. Soc. Rev.* **2010**, *39*, 2184.
[10] O. H. Kim, Y. H. Cho, S. H. Kang, H. Y. Park, M. Kim, J. W. Lim, D. Y. Chung, M. J. Lee, H. Choe, Y. E. Sung, *Nat. Commun.* **2013**, *4*, 2473.
[11] K. Yamamoto, T. Imaoka, W. J. Chun, O. Enoki, H. Katoh, M. Takenaga, A. Sonoi, *Nat. Chem.* **2009**, *1*, 397.
[12] E. Toyoda, R. Jinnouchi, T. Ohsuna, T. Hatanaka, T. Aizawa, S. Otani, Y. Kido, Y. Morimoto, *Angew. Chem. Int. Ed.* **2013**, *52*, 4137.
[13] J. Suntivich, H. A. Gasteiger, N. Yabuuchi, H. Nakanishi, J. B. Goodenough, Y. Shao-Horn, *Nat. Chem.* **2011**, *3*, 546.
[14] Y. Y. Liang, Y. G. Li, H. L. Wang, J. G. Zhou, J. Wang, T. Regier, H. J. Dai, *Nat. Mater.* **2011**, *10*, 780.
[15] K. P. Gong, F. Du, Z. H. Xia, M. Durstock, L. M. Dai, *Science* **2009**, *323*, 760.
[16] G. Wu, K. L. More, C. M. Johnston, P. Zelenay, *Science* **2011**, *332*, 443.
[17] S. B. Yang, X. L. Feng, X. C. Wang, K. Müllen, *Angew. Chem. Int. Ed.* **2011**, *50*, 5339.
[18] T. Toda, H. Igrashi, H. Uchida, M. Watanabe, *J. Electrochem. Soc.* **1999**, *146*, 3750.
[19] B. Hammer, J. K. Nørskov, *Adv. Catal.* **2000**, *45*, 71.
[20] J. Greeley, M. Mavrikakis, *Nat. Mater.* **2004**, *3*, 810.
[21] J. L. Zhang, M. B. Vukmirovic, K. Sasaki, A. U. Nilekar, M. Mavrikakis, R. R. Adžić, *J. Am. Chem. Soc.* **2005**, *127*, 12480.
[22] J. R. Kitchin, J. K. Nørskov, M. A. Barteau, J. G. Chen, *J. Chem. Phys.* **2004**, *120*, 10240.
[23] V. R. Stamenkovic, B. S. Mun, K. J. J. Mayrhofer, P. N. Ross, N. M. Markovic, J. Rossmeisl, J. Greeley, J. K. Nørskov, *Angew. Chem.* **2006**, *118*, 2963.
[24] M. Mavrikakis, B. Hammer, J. K. Nørskov, *Phys. Rev. Lett.* **1998**, *81*, 2819.
[25] P. Strasser, S. Koh, T. Anniyev, J. Greeley, K. More, C. F. Yu, Z. C. Liu, S. Kaya, D. Nordlund, H. Ogasawara, M. F. Toney, A. Nilsson, *Nat. Chem.* **2010**, *2*, 454.

[26] J. R. Kitchin, J. K. Nørskov, M. A. Barteau, J. G. Chen, *Phys. Rev. Lett.* **2004**, *93*, 156801.
[27] J. Greeley, I. E. L. Stephens, A. S. Bondarenko, T. P. Johansson, H. A. Hansen, T. F. Jaramillo, J. Rossmeisl, I. Chorkendorff, J. K. Nørskov, *Nat. Chem.* **2009**, *1*, 552.
[28] C. Wang, D. van der Vliet, K. L. More, N. J. Zaluzec, S. Peng, S. H. Sun, H. Daimon, G. F. Wang, J. Greeley, J. Pearson, A. P. Paulikas, G. Karapetrov, D. S. Strmcnik, N. M. Markovic, V. R. Stamenkovic, *Nano Lett.* **2011**, *11*, 919.
[29] D. L. Wang, H. L. L. Xin, R. Hovden, H. S. Wang, Y. C. Yu, D. A Muller, F. J. DiSalvo, H. D. Abruña, *Nat. Mater.* **2013**, *12*, 81.
[30] V. R. Stamenkovic, T. J. Schmidt, P. N. Ross, N. M. Markovic, *J. Phys. Chem. B* **2002**, *106*, 11970.
[31] V. R. Stamenkovic, B. Fowler, B. S. Mun, G. F. Wang, P. N. Ross, C. A. Lucas, N. M. Markovic, *Science* **2007**, *315*, 493.
[32] C. H. Cui, L. Gan, H. H. Li, S. H. Yu, M. Heggen, P. Strasser, *Nano Lett.* **2012**, *12*, 5885.
[33] J. B. Wu, L. Qi, H. J. You, A. Gross, J. Li, H. Yang, *J. Am. Chem. Soc.* **2012**, *134*, 11880.
[34] C. H. Cui, L. Gan, M. Heggen, S. Rudi, P. Strasser, *Nat. Mater.* **2013**, *12*, 765.
[35] R. Y. Wang, C. X. Xu, X. X. Bi, Y. Ding, *Energy Environ. Sci.* **2012**, *5*, 5281.
[36] W. A. Harrison, *Electronic Structure and the Properties of Solids*, Dover Publications, New York **1989**.
[37] S. Mukerjee, S. Srinivasan, M. P. Soriaga, J. McBreen, *J. Electrochem. Soc.* **1995**, *142*, 1409.
[38] S. J. Hwang, S. K. Kim, J. G. Lee, S. C. Lee, J. H. Jang, P. Kim, T. H. Lim, Y. E. Sung, S. J. Yoo, *J. Am. Chem. Soc.* **2012**, *134*, 19508.
[39] V. R. Stamenkovic, B. S. Mun, M. Arenz, K. J. J. Mayrhofer, C. A. Lucas, G. F. Wang, P. N. Ross, N. M. Markovic, *Nat. Mater.* **2007**, *6*, 241.
[40] D. F. van der Vliet, C. Wang, D. Tripkovic, D. Strmcnik, X. F. Zhang, M. K. Debe, R. T. Atanasoski, N. M. Markovic, V. R. Stamenkovic, *Nat. Mater.* **2012**, *11*, 1051.
[41] S. Chen, H. A. Gasteiger, K. Hayakawa, T. Tada, Y. Shao-Horn, *J. Electrochem. Soc.* **2010**, *157*, A82.
[42] V. R. Stamenkovic, B. S. Mun, K. J. J. Mayrhofer, P. N. Ross, N. M. Markovic, *J. Am. Chem. Soc.* **2006**, *128*, 8813.
[43] G. H. Jóhannesson, T. Bligaard, A. V. Ruban, H. L. Skriver, K. W. Jacobsen, J. K. Nørskov, *Phys. Rev. Lett.* **2002**, *88*, 255506.
[44] R. W. Cahn, P. Haasen, *Physical Metallurgy,* Elsevier Sci, Amsterdam **1996**.
[45] J. Erlebacher, *J. Electrochem. Soc.* **2004**, *151*, C614.
[46] Q. Jiang, S. H. Zhang, J. C. Li, *Solid State Commun.* **2004**, *130*, 581.
[47] H. Connor, *Platinum Metals Rev.* **1962**, *6*, 136.
[48] L. Y. Chen, H. Guo, T. Fujita, A. Hirata, W. Zhang, A. Inoue, M. W. Chen, *Adv. Funct. Mater.* **2011**, *21*, 4364.
[49] Z. H. Zhang, Y. Wang, Z. Qi, W. H. Zhang, J. Y. Qin, J. Frenzel, *J. Phys. Chem. C* **2009**, *113*, 12629.
[50] J. Erlebacher, M. J. Aziz, A. Karma, N. Dimitrov, K. Sieradzki, *Nature* **2001**, *410*, 450.
[51] H. Galinski, T. Ryll, L. Schlagenhauf, F. Rechberger, S. Ying, L. J. Gauckler, M. Döbeli, *Phys. Rev. Lett.* **2011**, *107*, 225503.
[52] J. Snyder, T. Fujita, M. W. Chen, J. Erlebacher, *Nat. Mater.* **2010**, *9*, 904.
[53] U. A. Paulus, A. Wokaun, G. G. Scherer, T. J. Schmidt, V. R. Stamenkovic, V. Radmilovic, N. M. Markovic, P. N. Ross, *J. Phys. Chem. B* **2002**, *106*, 4181.
[54] X. Y. Lang, H. Y. Fu, C. Hou, G. F. Han, P. Yang, Y. B. Liu, Q. Jiang, *Nat. Commun.* **2013**, *4*, 2169.
[55] J. Kibsgaard, Y. Gorlin, Z. B. Chen, T. F. Jaramillo, *J. Am. Chem. Soc.* **2012**, *134*, 7758.
[56] M. Escudero-Escribano, A. Verdaguer-Casadevall, P. Malacrida, U. Grønbjerg, B. P. Knudsen, A. K. Jepsen, J. Rossmeisl, I. E. L. Stephens, I. Chorkendorff, *J. Am. Chem. Soc.* **2012**, *134*, 16476.
[57] P. Vanýsek, in *CRC Handbook of Chemistry and Physics* (Ed.: D. R. Lide) Taylor and Francis, Boca Raton, FL **2007**, ch. 8, p 20.
[58] D. Briggs, M. P. Seah, *Practical Surface Analysis, 2nd ed.; Volume 1: Auger and X-ray Photoelectron Spectroscopy*, Wiley, New York **1990**.
[59] B. Richter, H. Kuhlenbeck, H. J. Freund, P. S. Bagus, *Phys. Rev. Lett.* **2004**, *93*, 026805.
[60] S. J. Yoo, S. J. Hwang, J. G. Lee, S. C. Lee, T. H. Lim, Y. E. Sung, A. Wieckowski, S. K. Kim, *Energy Environ. Sci.* **2012**, *5*, 7521.
[61] Y. Wu, D. Wang, G. Zhou, R. Yu, C. Chen, Y. Li, *J. Am. Chem. Soc.* **2014**, *136*, 11594.
[62] G. Wang, B. Huang, L. Xiao, Z. Ren, H. Chen, D. Wang, H. D. Abruna, J. Lu, L. Zhuang, *J. Am. Chem. Soc.* **2014**, *136*, 9643.
[63] M. Wakisaka, S. Mitsui, Y. Hirose, K. Kawashima, H. Uchida, M. Watanabe, *J. Phys. Chem. B* **2006**, *110*, 23489.
[64] J. H. Bae, J. H. Han, T. D. Chung, *Phys. Chem. Chem. Phys.* **2012**, *14*, 448.

DOI: 10.1002/adfm.201401868